

ARTICLE

<https://doi.org/10.1038/s42005-020-0290-x>

OPEN

Resonant tunnelling into the two-dimensional subbands of InSe layers

Zakhar R. Kudrynskiy ¹, James Kerfoot¹, Debarati Mazumder¹, Mark T. Greenaway ^{1,2}, Evgeni E. Vdovin³, Oleg Makarovskiy¹, Zakhar D. Kovalyuk⁴, Laurence Eaves¹, Peter H. Beton ¹ & Amalia Patanè^{1*}

Two-dimensional (2D) van der Waals (vdW) crystals have attracted considerable interest for digital electronics beyond Si-based complementary metal oxide semiconductor technologies. Despite the transformative success of Si-based devices, there are limits to their miniaturization and functionalities. Here we realize a resonant tunnelling transistor (RTT) based on a 2D InSe layer sandwiched between two multilayered graphene (MLG) electrodes. In the RTT the energy of the quantum-confined 2D subbands of InSe can be tuned by the thickness of the InSe layer. By applying a voltage across the two MLG electrodes, which serve as the source and drain electrodes to the InSe, the chemical potential in the source can be tuned in and out of resonance with a given 2D subband, leading to multiple regions of negative differential conductance that can be additionally tuned by electrostatic gating. This work demonstrates the potential of InSe and InSe-based RTTs for applications in quantum electronics.

¹School of Physics and Astronomy, University of Nottingham, Nottingham NG7 2RD, UK. ²Department of Physics, Loughborough University, Loughborough, LE11 3TU, UK. ³Institute of Microelectronics Technology and High Purity Materials, RAS, Chernogolovka 142432, Russia. ⁴Institute for Problems of Materials Science, The National Academy of Sciences of Ukraine, Chernivtsi Branch, Chernivtsi 58001, Ukraine. *email: amalia.patane@nottingham.ac.uk

Heterostructures based on two-dimensional (2D) van der Waals (vdW) crystals^{1–3}, such as graphene, hexagonal boron nitride (hBN), and metal mono- (e.g., InSe, GaSe...) and di-chalcogenide (e.g., SnSe₂, MoS₂...) layers have physical properties that may overcome some of the technological limitations of traditional covalent semiconductors⁴. Beyond their versatility for a wide range of band structure-engineered devices by stacking and/or twisting the layers, these structures can be also readily transferred onto substrates that are compatible with the well-established complementary metal–oxide–semiconductor (CMOS) device fabrication processes used in modern integrated circuits for digital logic, image sensors and transceivers. In recent years, different types of tunnel field effect transistors (TFET) based on vdW crystals have emerged, stimulating research of fundamental and applied interest^{5–13}. These devices include the graphene/insulator/graphene TFET with a region of negative differential conductance (NDC) in the current–voltage characteristics due to resonant tunnelling⁸. Similar TFET structures based on transition metal di-chalcogenides (TMDs) rather than graphene layers have been also suggested and studied theoretically, revealing improved transport characteristics due to qualitative differences in the band structure of these materials compared to graphene⁹. Furthermore, Esaki-type tunnel diodes¹⁰ have demonstrated the potential of 2D materials for transistors with a low subthreshold swing and NDC by band-to-band tunnelling of carriers through the forbidden energy gap of a vdW heterojunction^{11–13}.

Here, we report on a different type of TFET, a resonant tunneling transistor (RTT), which exhibits multiple regions of NDC. These device structures exploit the tunnelling of charge carriers from a source of electrons into the distinct 2D subband states of an InSe vdW crystal a few atomic layers thick. We use important features of the RTT: due to strong quantum confinement of the light effective mass electrons¹⁴, the energy of the 2D subbands can be tuned by varying the thickness of the InSe layer. By applying a voltage, V_{SD} , across two multilayer graphene (MLG) electrodes, which serve as the source (S) and drain (D) electrodes to the InSe layer, the chemical potential in the source can be tuned in and out of resonance with a given 2D subband, leading to a peak in the current–voltage (I – V_{SD}) characteristics and a region of NDC. Multiple regions of NDC can be thus induced by tunnelling into consecutive 2D subbands of InSe, whose number increases with the number of InSe layers. Our findings suggest prospects for further research avenues and applications. InSe-based RTTs could aid the development of multivalued logic and frequency multiplication. Furthermore, intersubband transitions of individual InSe layers or repeated multilayered stacks could be exploited in photon sources and detectors. InSe offers exciting possibilities for these technological developments due to its high room temperature electron mobility and its tuneable band gap and energy subbands^{14–16}.

Results

Resonant tunnelling transistors with NDC. Figure 1a illustrates the schematic layered structure and an optical image of a typical device formed by dry transfer¹⁷ of exfoliated MLG, hBN, and InSe on a SiO₂/Si substrate (details of the sample preparation and measurement techniques are described in the Methods section and Supplementary Note 1). In this device, the InSe layer has an in-plane area of $\sim 100 \mu\text{m}^2$ and thickness $t \sim 8 \text{ nm}$ (ten layers of InSe). A voltage (V_{SD}) is applied to the top MLG-electrode relative to the bottom to align different 2D subbands of InSe to the chemical potential in the source. The Si-substrate serves as a gate electrode and the gate voltage, V_g , is used to adjust the chemical potential in the adjacent/bottom MLG. Figure 1b shows

the current–voltage I – V_{SD} curve at a measurement temperature, $T = 2.0 \text{ K}$, and $V_g = 0$. For $|V_{SD}| \lesssim 0.5 \text{ V}$, the tunnel current remains small ($< 10 \text{ pA}$) for both positive and negative applied voltages. However, for $V_{SD} > 0.5 \text{ V}$, the current increases rapidly and the I – V_{SD} curve reveals a sequence of resonant features. Pronounced peaks in the I – V_{SD} can be seen over an extended range of V_{SD} and are followed at higher bias ($|V_{SD}| > 1.1 \text{ V}$) by weaker resonances. These resonances, labelled S_1, S_2, \dots in Fig. 1b can be seen more clearly in the differential conductance, $G = dI/dV_{SD}$, plot shown in Fig. 1c. We attribute each resonance to the threshold of resonant tunnelling through a quantized 2D subband of the InSe layer when the energy of the subband minimum aligns with the chemical potential of the MLG-source electrode (inset of Fig. 1c, d). The asymmetry of the I – V_{SD} curve with respect to positive and negative voltages suggests that the two interfaces of the InSe with the two MLG-electrodes are different. The resonances can be observed more clearly when electrons tunnel from the bottom to the top MLG ($V_{SD} > 0$), suggesting that the InSe layer forms a cleaner interface with the bottom MLG. This asymmetry is likely to arise from the lower quality of the top surface of InSe, which tends to be more contaminated than the bottom surface due to the use of polymer stamps for the exfoliation of InSe.

The resonances are observed over a wide temperature range (Fig. 2a–b): on increasing the temperature from $T = 2 \text{ K}$ to 144 K , the resonances shift to lower values of V_{SD} and tend to broaden; they cannot be resolved clearly at $T = 300 \text{ K}$ (inset of Fig. 2a). We assign this behavior to two main effects: the thermal broadening of the electron distribution in the MLG-source; secondly, the resonant subband states of the InSe layer are effectively broadened due to scattering of charge carriers by thermally excited lattice vibrations. This phenomenon is further examined in the Discussion section.

Tunnelling into the 2D subbands of InSe. InSe-based devices can be designed and fabricated with different thickness, t , of the InSe layer and hence with different subband energies. Figure 3a shows the t -dependence of the energy minima of the InSe subbands. Here, we use the simplifying assumption that the electrons are confined by a square quantum well (QW) potential of infinite height, i.e., $E_n = n^2 \hbar^2 / 8t^2 m_c^e$, where n is an integer, $m_c^e = 0.08m_e$ is the electron effective mass for motion along the c -axis in bulk InSe¹⁸, and m_e is the free electron mass. The calculated energy separation, ΔE_{2-1} , between the lowest two subbands decreases from hundreds of meV to a few meV with increasing t from 2 to 20 layers (Fig. 3a). Figure 3b shows the corresponding t -dependence of the band-edge exciton recombination energy, i.e., $E_X = E_X^{3D} + \hbar^2 / 8t^2 \mu_c^{\text{ex}}$, where $E_X^{3D} = 1.25 \text{ eV}$ is the value of E_X for bulk InSe at $T = 300 \text{ K}$, $\mu_c^{\text{ex}} = 1/[1/m_c^e + 1/m_c^h]$ is the reduced exciton mass, and $m_c^h = 0.17m_e$ is the hole effective mass¹⁹. Similar dependences of E_X and ΔE_{2-1} on t were predicted by density functional theory^{20,21}, thought with larger deviations from the simple QW model at smaller t ²¹.

We now consider the measured I – V_{SD} characteristics of three devices with different InSe layer thicknesses $t = 8, 10,$ and 19 layers, as estimated from the photoluminescence (PL) spectra of these three samples at $T = 300 \text{ K}$ (inset of Fig. 3b). The PL peak energy corresponds to that of the band-edge exciton^{21,22} and is very sensitive to the layer thickness: it increases from $E_X \sim 1.28 \text{ eV}$ for $t = 19$ layers to $E_X \sim 1.39 \text{ eV}$ for $t = 8$ layers. Figure 3c shows the I – V_{SD} and G – V_{SD} curves of these three devices, revealing that the current and voltage spacing between consecutive resonances increases with decreasing t . We note that no resonances were observed in the device with $t = 19$ layers or in other devices with thicker layers. For these devices with a relatively thicker InSe

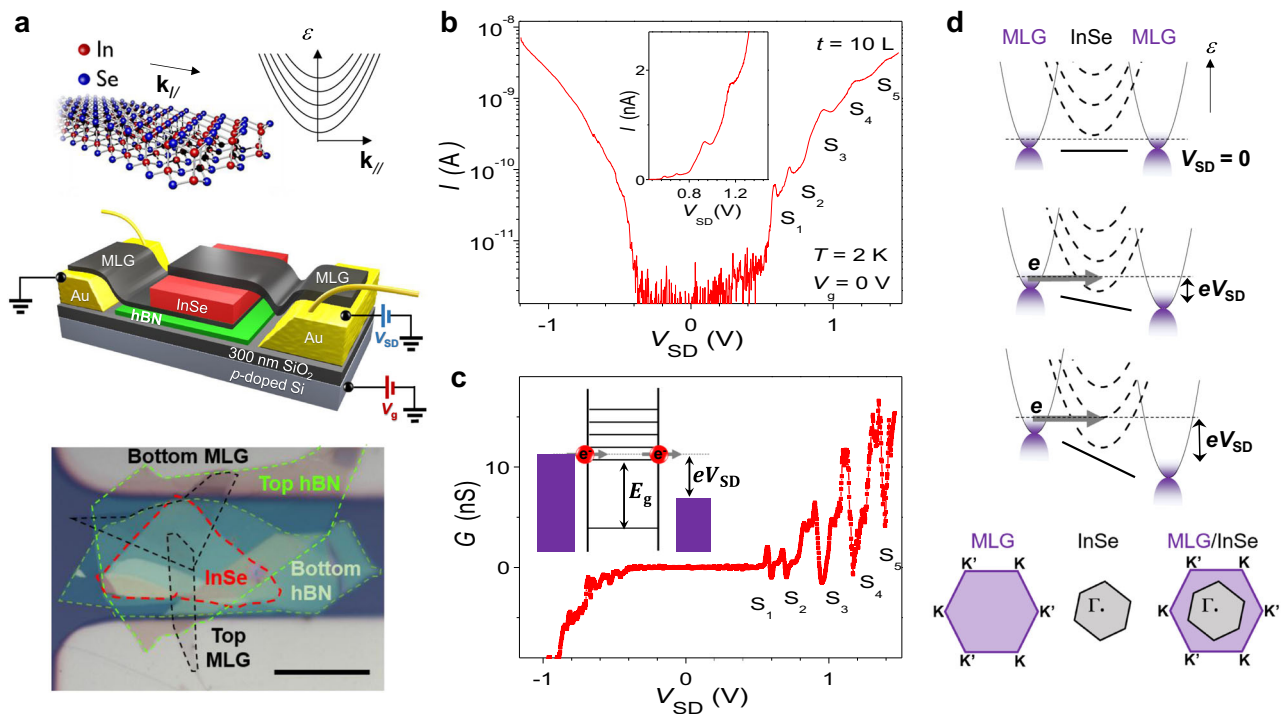


Fig. 1 InSe-based resonant tunnelling transistors with NDC. **a** Optical image (scale bar: 20 μ m) and schematic of an InSe-based resonant tunnelling transistor. The device is constructed by dry transfer of individual layers (e.g., InSe, hexagonal boron nitride (hBN), and multilayer graphene (MLG)) onto a SiO₂/Si substrate and is encapsulated by hBN. The top insets show the crystal structure of single-layer InSe and the in-plane energy dispersion of the two-dimensional (2D) InSe subbands. **b** Current-voltage, I - V_{SD} , characteristics of a device with ten-layers (10 L) InSe at a gate voltage $V_g = 0$ V and temperature $T = 2$ K. Inset: zoom in of the I - V_{SD} curve in forward bias. **c** Differential conductance, G - V_{SD} , curve at $V_g = 0$ V and $T = 2$ K. Inset: sketch of the tunnelling of electrons from a MLG-electrode (source) into the 2D subbands of InSe. **d** Schematic of tunnelling of electrons from a MLG-electrode (source) into the 2D subbands of InSe and into MLG (drain) for an increasing source-to-drain voltage, V_{SD} . Bottom inset: Brillouin zone of InSe and MLG.

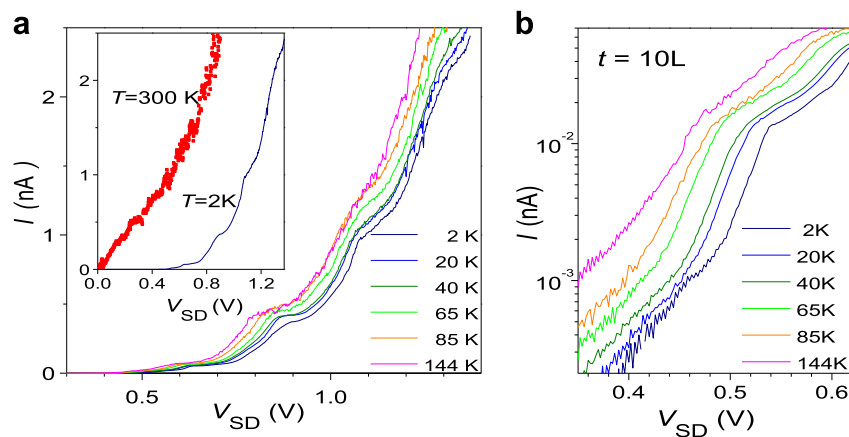


Fig. 2 Temperature dependence of the transport characteristics. **a** Current-voltage characteristics, I - V_{SD} , of a device with ten-layers InSe at a gate voltage $V_g = 0$ V and at different temperatures T . The inset compares the I - V_{SD} curves at $T = 300$ K and 2 K. **b** I - V_{SD} curves from part (a) in the low voltage region.

layer, the I - V_{SD} also reveal a distinct temperature dependence: the conductivity exhibits a thermally activated behavior, suggestive of thermal emission of electrons from shallow donor and defect states in InSe (Supplementary Fig. 2).

To estimate the energy spacing between the 2D subbands, we examine the V_g -dependence of the main conductance peaks S_1, S_2, S_3, \dots in the device with ten-layers InSe. As shown in Fig. 4a, an increase of V_g decreases the V_{SD} -position of these peaks. This behavior can be seen more clearly in the $G(V_{SD}, V_g)$ color map of Fig. 4b. Here, the dashed black lines illustrate that for a sufficiently large applied gate voltage, all the S_n -resonances

exhibit a similar shift with the applied gate voltage (e.g., $dV_{SD}/dV_g \sim -0.005$). The spacing between the first two resonances S_1 and S_2 is $\Delta V_{SD} \sim 0.2$ V at $V_g = +30$ V. This is in good agreement with the calculated energy spacing ΔE_{1-2} between the lowest electron energy subbands of InSe shown in Fig. 3a. Decreasing the layer thickness from 10 to 8 layers increases the measured value of ΔV_{SD} from ~ 0.2 V to ~ 0.3 V (Fig. 3c). As can be seen in Fig. 3a, this value of ΔV_{SD} is in agreement with the calculated energy spacing ΔE_{2-1} , which increases from $\Delta E_{2-1} = 0.20$ – 0.32 eV with decreasing t from 10 to 8 layers. Thus our data suggest a leverage factor $f = e(dV_{SD}/dE) \approx 1$, where dV_{SD} is the

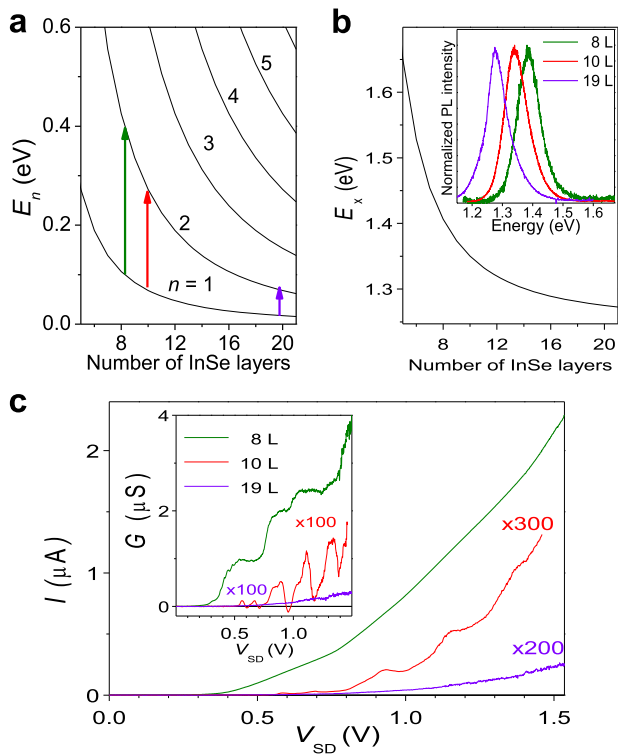


Fig. 3 2D subbands in InSe. **a, b** Calculated dependence of the subbands **a** and exciton recombination **b** energies on the number of InSe layers. The arrows in part **a** show the energy spacing between the lowest two subbands for three specific layer thicknesses. The inset in part **b** shows the normalized photoluminescence spectra of devices with 8, 10, and 19 layers (L) of InSe at $T = 300$ K. **c** Current–voltage, I – V_{SD} , characteristics of devices with different InSe layer thickness ($t = 8, 10,$ and 19 layers) at the gate voltage $V_g = 0$ V and $T = 2$ K. Inset: differential conductance, G – V_{SD} , plots for devices with thickness $t = 8, 10,$ and 19 layers. The multiplication factor indicates the number by which each curve has been multiplied to facilitate a comparison of different samples.

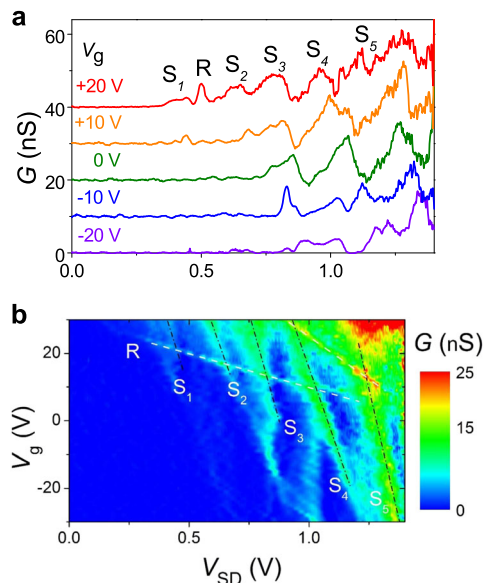


Fig. 4 Electrostatic gating of the NDC. **a** Differential conductance, G – V_{SD} , curves at different gate voltages, V_g , at a temperature $T = 2$ K for a device with ten-layers InSe (curves are offset for clarity). **b** Color map of G versus V_{SD} and V_g at $T = 2$ K. Black and white lines identify different resonances.

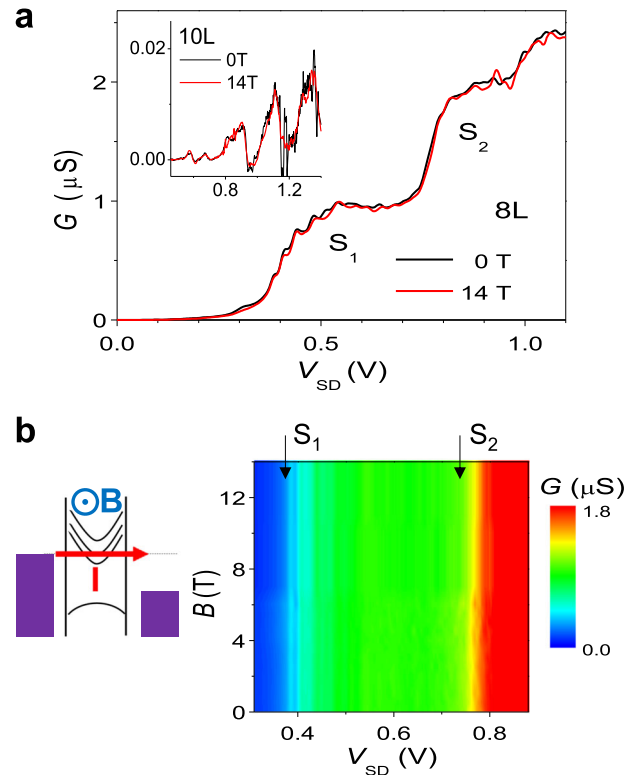


Fig. 5 Magneto-tunnelling studies. **a** Differential conductance, G – V_{SD} , curves at applied magnetic fields $B = 0$ and 14 T for devices with eight-layers (main panel) and ten-layers (inset) InSe. In both cases the gate voltage is $V_g = 0$ V, the temperature is $T = 2$ K and the magnetic field is applied perpendicular to the direction of the current. **b** $G(B, V_{SD})$ color map for the device with eight-layers InSe ($T = 2$ K). The inset is a schematic of the injection of electrons from the electrode into the subbands of InSe. The parabolas illustrate the in-plane energy dispersion of the subbands.

incremental change of the applied voltage corresponding to a change in energy dE of a particular subband. A value of $f \approx 1$ is in line with the observation of electroluminescence from our devices when the chemical potentials in the source and drain differs by an energy $\Delta E = eV_{SD}$ that is approximately equal to the exciton recombination energy in the InSe layer, i.e., $eV_{SD} \sim E_X$ (Supplementary Note 2). This is also consistent with a simple electrostatic model of our devices that gives f -values between 1 and 2, depending on the applied gate voltage (Supplementary Note 3).

We now examine additional characteristic features of these RTTs. As shown in Fig. 4a for the device with $t = 10$ layers, at $V_g \sim +20$ V, a narrow resonance, R, emerges at $V_{SD} \sim +0.5$ V. This can be seen more clearly in the $G(V_{SD}, V_g)$ color map of Fig. 4b. Here, the white lines highlight the shift and splitting of the narrow R-resonance. The emergence of this additional narrow feature in the transport characteristics of our devices is similar to recent observations of resonant electron tunneling through localized states due to defects in hBN²³. The stronger dependence of R on V_g ($dV_{SD}/dV_g \sim -0.05$) compared to that of S_n ($dV_{SD}/dV_g \sim -0.005$) suggests that R arises from carrier tunneling into the states of a localized defect close to the bottom gate electrode. Similar narrow resonances can be seen in the same device under negative applied gate voltages and $V_{SD} \sim +1.0$ V (Fig. 4b). Also, close inspection of the G – V_{SD} plots of different devices reveals that the main S_n -resonances can comprise additional weak features closely spaced in energy (Fig. 5a). This quasi-regular modulation of the current is weakly affected by temperature, although the increasing noise and broadening of the

resonances prevent its clear observation above $T = 100$ K (Supplementary Fig. 6). The positions of the main resonances S_n and that of the additional features are only weakly affected by a magnetic field (B) applied perpendicular to the direction of the current (Fig. 5a–b). These dependences are further discussed below.

Discussion

Our devices based on a few layers of InSe sandwiched between two MLG electrodes differ in several important aspects from the well-established resonant tunnelling diodes (RTDs) based on heterostructures, in which the crystal lattices of the component layers are aligned and lattice matched. A typical example is the RTD in which two (AlGa)As tunnel barriers enclose a GaAs QW with the source and drain contacts composed of doped GaAs²⁴. The GaAs–AlGaAs RTDs are ideally suited to conserve both the energy and momentum of the tunnelling carriers so that strong resonant peaks and extended regions of NDC with high peak-to-valley ratios are observed.

In our devices, the hexagonal lattices of InSe ($a = 4.002$ Å) and graphene ($a = 2.46$ Å) are strongly mismatched ($\sim 60\%$) and are not intentionally aligned. Furthermore, in undoped graphene and MLG the occupied states are located around the K and K' points of the hexagonal Brillouin zone, whereas the conduction band edge of InSe is at the Γ -point (Fig. 1d). For electron tunneling from MLG to InSe, an electron must overcome the large momentum difference between the K-(K'-) and Γ -points. This can be provided by the scattering potential at the InSe–graphene interface due to the large lattice mismatch of the InSe and graphene layers, and/or disorder in the layers. This is analogous to the situation encountered in previous studies of almost lattice-matched graphene–hBN–graphene tunnel transistors, in which the lattices of the graphene electrodes were misaligned. This misalignment gives rise to a difference between the in-plane momenta of the initial and final states of electrons tunnelling between the two graphene layers. In this case, the in-plane scattering allows energy-conserving resonant tunnelling to occur even when the wave vectors of the tunnelling electrons in the collector and emitter are different⁸. As shown in the Supplementary Note 4, our measured region of NDC in the MLG–InSe–MLG heterostructures can be explained in terms of a similar model.

As $|V_{SD}|$ increases, electrons tunnel through the states of distinct InSe subbands or states with increasing in-plane momentum within the same subband. When, with increasing $|V_{SD}|$, an additional subband becomes resonantly aligned with the chemical potential in the source, an additional resonant feature appears in $I-V_{SD}$, along with a further increase of the current. Although each 2D subband should produce a distinct peak in $I-V_{SD}$, the overlapping contributions from different subbands acts to increase the valley current between adjacent resonances, giving rise to a steadily increasing monotonic background current. Furthermore, as can be seen in the $I-V_{SD}$ plots of Fig. 1b, the current increases by two orders of magnitude going from S_1 to S_5 . This increase can be understood by reference to the schematic diagram in Fig. 1d. With increasing voltage, there is an increasing number of filled and empty states in the source and drain electrodes, respectively. Thus, the current and the amplitude of the differential conductance increase with increasing V_{SD} .

We note that InSe has a much smaller band gap energy than that of hBN, which was previously used to realize TFETs^{5,8,23}. The band alignment of InSe and hBN with respect to the Dirac points of graphene (or the conduction band of MLG) is also quite different; whereas the Dirac point lies almost in the middle of the band gap of hBN, it is positioned closer to the conduction band edge of InSe²⁵. A MLG–InSe–MLG heterostructure therefore has

a band alignment that takes the form shown schematically in Fig. 1d. By reducing the thickness of the InSe layer the energy gap of InSe can be increased due to quantum confinement, increasing the effective height of the InSe tunnel barrier. This also changes the number of 2D subbands and their energy spacing. Thus, in these RTTs, the InSe layer thickness can control both the tunnelling rate of the charge carriers and the resonant enhancement of the current through 2D subbands whose energy position is very sensitive to quantum confinement. An additional feature of interest is that, despite the absence of a real energy barrier between the MLG and InSe layers, the subband states of the InSe layer are sufficiently well defined to produce prominent resonant features in the current–voltage characteristics. The difference between the $I-V_{SD}$ characteristics of the eight-layer and ten-layer devices suggests that aside the transmission of electrons through a barrier of finite length and height, additional mechanisms contribute to the transport characteristics of these devices. For example, impurities and/or interface disorder are likely to affect both the magnitude of the current and the broadening of the resonances, with a larger current and/or broader resonances in layers that are more disordered due to scattering (Supplementary Note 4 and Supplementary Fig. 8).

As shown in Fig. 5a, a magnetic field of up to $B = 14$ T applied perpendicular to the direction of the current (e.g., parallel to the c -axis) has almost no effect on the amplitude and voltage position of the S_n -resonances in the devices with eight and ten-layers InSe. This weak dependence on B is consistent with the strong quantum confinement of electrons along the c -axis: at $B = 14$ T, the magnetic length $l = \sqrt{\hbar/eB}$ is equal to 6.8 nm, comparable to or smaller than the thickness of the InSe layer (~ 6 and 8 nm in the devices with eight and ten-layers InSe, respectively). Furthermore, for this orientation of magnetic field, when an electron tunnels from the source into a 2D subband, it acquires an additional in-plane wave vector $\Delta k = -eBs/\hbar$ ²⁴ due to the Lorentz force exerted on the electrons as they tunnel. Here, s is the effective tunneling length from the source to the centre of the InSe layer. Electrons that tunnel from states close to the K-points of the MLG into states near the Γ -point of the InSe layer require a much larger change of in-plane wave vector than that due to the Lorentz force. As discussed before, this can be provided by the scattering potential at the InSe–graphene interface. For $s = t/2 = 3$ nm and $B = 14$ T, we estimate $k = eB_{\perp}s/\hbar = 6.4 \times 10^7$ m⁻¹, corresponding to a change in energy $\Delta\varepsilon = \hbar^2 k^2 / 2m_{||}^e \sim 1$ meV. This weak dispersion is due to the relatively large effective mass of the conduction electrons in the layer plane ($m_{||}^e = 0.14m_e$)²¹. Thus, even with magnetic fields of up to 14 T, the change in the in-plane wave vector k (and corresponding kinetic energy $\Delta\varepsilon$) of the tunnelling electron is too small to detect a voltage shift $\Delta V_{SD} = \varepsilon(\Delta k)/e$ or change in amplitude of the resonances in the $I-V_{SD}$ characteristics.

Finally, we attribute the temperature dependence of the differential conductance peaks (Fig. 2) to the thermal broadening of the electron distribution around the Fermi energy in the MLG-source and to phonon-assisted tunneling. The energy of the optical phonon modes in InSe is in the range 14–30 meV²⁶. When these lattice vibrations are thermally activated, they inelastically scatter the tunneling electrons. In turn, this broadens the resonances and shifts their position to lower voltages with increasing T (Fig. 2). Elastic scattering mechanisms also influence the tunnel current. In particular, fluctuations of the electrical conductance characteristics can be seen in our devices (Fig. 5a). This can vary from sample to sample due to scattering sites at the interfaces, local electric fields arising from surface dipoles due to the local atomic structure and charge distribution at the surface of the layers (Supplementary Fig. 6). A better understanding and

control of these factors are required in order to optimize the performance of the RTTs.

In conclusion, we have realized vertical tunnel transistors with an InSe layer between two MLG contacts. Within the wide family of vdW crystals, InSe provides a very promising conduction channel due to the strong dependence of its 2D energy subbands on quantum confinement, offering a route to the modulation of electrical properties. Electron tunneling into consecutive 2D subbands of InSe leads to multiple regions of NDC that can be tuned by electrostatic gating. Our devices could provide the foundation for further technologies, such as low-power consumption transistors and broad-band sources and detectors compatible with existing photonic and CMOS technologies. RTTs could offer opportunities to perform more logic operations per transistor than conventional transistors, providing a foundation for multivalued logic and frequency multiplication^{27–29}. Recent observations of intersubband transitions by near-field optics in TMDs³⁰ have demonstrated the potential of 2D intersubband transitions for optoelectronics. The InSe-based RTTs demonstrated in this work has the potential for a broad spectral range with intraband transitions tuneable from the near infrared in a bilayer InSe to the far-infrared/terahertz range in thicker InSe films. In particular, by suitable design of the layer thicknesses, it may be possible to engineer population inversion between the subbands and tune the photon emission, as done in quantum cascade lasers based on traditional semiconductors³¹.

Methods

Materials. Our InSe crystals were grown using the Bridgman method from a polycrystalline melt of $\text{In}_{1.03}\text{Se}_{0.97}$. The primitive unit cell contains three InSe layers, each of which has a thickness of 8.320 Å and consists of four covalently bonded monoatomic sheets in the sequence Se–In–In–Se (Fig. 1a); along the *c*-axis, the primitive unit cell has a lattice constant of $c = 24.961$ Å and, within each *a*–*b* plane, atoms form hexagons with lattice parameter $a = 4.002$ Å. In its bulk form, InSe contains native donors due to In-interstitial atoms. From Hall effect measurements on bulk InSe at $T = 300$ K, we estimate an electron density $n \sim 10^{21} \text{ m}^{-3}$, an electron mobility $\mu = 0.1 \text{ m}^2 \text{ V}^{-1} \text{ s}^{-1}$, and a Fermi energy $E_F \sim 0.21$ eV below the conduction band minimum.

Device fabrication. Our TFETs are assembled on a conventional SiO_2/Si substrate (SiO_2 layer thickness of 300 nm) using mechanically exfoliated MLG, hBN, and InSe flakes. These are deposited sequentially onto preprepared metal contacts, Au/Cr (30 nm/10 nm), using a dry transfer method under ambient conditions¹⁵. Flakes of hBN, MLG, and InSe are first exfoliated onto polydimethylsiloxane (PDMS) from a low-tack, low-residue tape and identified using transmission and reflection mode optical microscopy. Then, using a micromanipulator stage, exfoliated flakes on PDMS are aligned to the metal contacts/predeposited flakes and brought into contact. The PDMS is then slowly retracted in order to sequentially deposit a bottom hBN flake, a MLG electrode, few layer InSe, a top MLG electrode, and an encapsulating hBN flake. The latter protects the whole heterostructure from contamination during long-term exposure to atmospheric conditions. The thickness of the MLG electrodes in different devices is between 10 and 18 layers.

Techniques. Magneto-transport measurements are conducted with the device mounted inside a superconducting magneto-cryostat at magnetic fields B of up to 14 T applied perpendicular to the direction of the current. The low-temperature transport characteristics reveal an electrical noise of ~ 1 pA. This is mainly limited by the measurement equipment. As the temperature increases, the source of noise is from both the device (e.g., thermal noise) and equipment. The experimental setup for the μPL spectroscopy studies at room temperature comprises lasers ($\lambda = 633$ nm and 405 nm), a *x*–*y*–*z* motorized stage and an optical confocal microscope system equipped with a 0.5-m long monochromator with 150 and 1200 g/mm gratings. The laser beam is focused to a diameter $d \sim 1$ μm using a 100 \times objective. The signal is detected by a Si-charge-coupled device camera. The optical studies are performed at low excitation power ($P < 10^{-4}$ W) to avoid excessive heating. Images of the layers' topography were acquired by atomic force microscopy (AFM, MFP-3D) in non-contact mode under ambient conditions.

Data availability

All relevant data that support the findings of this study are available in Nottingham Research Data Management Repository (<https://doi.org/10.17639/nottingham>).

Received: 10 September 2019; Accepted: 7 January 2020;

Published online: 21 January 2020

References

- Geim, A. K. & Grigorieva, I. V. Van der Waals heterostructures. *Nature* **499**, 419–425 (2013).
- Novoselov, K. S., Mishchenko, A., Carvalho, A. & Castro Neto, A. H. 2D materials and van der Waals heterostructures. *Science* **353**, 461–473 (2016).
- Mounet, N. et al. Two-dimensional materials from high-throughput computational exfoliation of experimentally known compounds. *Nat. Nanotechnol.* **13**, 246–252 (2018).
- Fiori, G. et al. Electronics based on two-dimensional materials. *Nat. Nanotechnol.* **9**, 768–779 (2014).
- Britnell, L. et al. Field-effect tunneling transistor based on vertical graphene heterostructures. *Science* **335**, 947–950 (2012).
- Feenstra, R. M., Jena, D. & Gu, G. Single-particle tunneling in doped graphene-insulator-graphene junctions. *J. Appl. Phys.* **111**, 043711 (2012).
- Zhao, P., Feenstra, R. M., Gu, G. & Jena, D. SymFET: a proposed symmetric graphene tunneling field-effect transistor. *IEEE Trans. Electron Devices* **60**, 951–957 (2013).
- Britnell, L. et al. Resonant tunnelling and negative differential conductance in graphene transistors. *Nat. Commun.* **4**, 1794 (2013).
- Campbell, P. M., Tarasov, A., Joiner, C. A., Ready, W. J. & Vogel, E. M. Enhanced resonant tunneling in symmetric 2D semiconductor vertical heterostructure transistors. *ACS Nano* **9**, 5000–5008 (2015).
- Esaki, L. New phenomenon in narrow germanium p–n junctions. *Phys. Rev.* **109**, 603 (1958).
- Yan, R. et al. Esaki diodes in van der Waals heterojunctions with broken-gap energy band alignment. *Nano Lett.* **15**, 5791–5798 (2015).
- Roy, T. et al. Dual-gated $\text{MoS}_2/\text{WSe}_2$ van der Waals tunnel diodes and transistors. *ACS Nano* **9**, 2071–2079 (2015).
- Liu, X. et al. Modulation of quantum tunneling via a vertical two-dimensional black phosphorus and molybdenum disulfide p–n junction. *ACS Nano* **11**, 9143–9150 (2017).
- Mudd, G. W. et al. Tuning the bandgap of exfoliated InSe nanosheets by quantum confinement. *Adv. Mater.* **25**, 5714–5718 (2013).
- Bandurin, D. A. et al. High electron mobility, quantum Hall effect and anomalous optical response in atomically thin InSe. *Nat. Nanotechnol.* **12**, 223–227 (2016).
- Brotens-Gisbert, M. et al. Nanotexturing to enhance photoluminescent response of atomically thin indium selenide with highly tunable band gap. *Nano Lett.* **16**, 3221–3229 (2016).
- Castellanos-Gomez, A. et al. Deterministic transfer of two-dimensional materials by all-dry viscoelastic stamping. *2D Mater.* **1**, 011002 (2014).
- Kress-Rogers, E., Nicholas, R., Portal, J. C. & Chevy, A. Cyclotron resonance studies on bulk and two-dimensional conduction electrons in InSe. *Solid State Commun.* **44**, 379–383 (1982).
- Ferrer-Roca, Ch., Segura, A., Andrés, M. V., Pellicer, J. & Muñoz, V. Investigation of nitrogen-related acceptor centers in indium selenide by means of photoluminescence: determination of the hole effective mass. *Phys. Rev. B* **55**, 6981–6987 (1997).
- Magorrian, S. J., Ceferino, A., Zólyomi, V. & Fal'ko, V. I. Hybrid $k \cdot p$ tight-binding model for intersubband optics in atomically thin InSe films. *Phys. Rev. B* **97**, 165304 (2018).
- Mudd, G. W. et al. The direct-to-indirect band gap crossover in two-dimensional van der Waals indium selenide crystals. *Sci. Rep.* **6**, 39619–39629 (2016).
- Shubina, T. V. et al. InSe as a case between 3D and 2D layered crystals for excitons. *Nat. Commun.* **10**, 3479 (2019).
- Greenaway, M. et al. Tunnel spectroscopy of localised electronic states in hexagonal boron nitride. *Commun. Phys.* **1**, 94 (2018).
- Hayden, R. K. et al. Probing the hole dispersion curves of a quantum well using resonant magneto-tunneling spectroscopy. *Phys. Rev. Lett.* **66**, 1749–1752 (1991).
- Mudd, G. W. et al. High broad-band photoresponsivity of mechanically formed InSe–graphene van der Waals heterostructures. *Adv. Mater.* **27**, 3760–3766 (2015).
- Kuroda, N. & Nishina, Y. Resonant Raman scattering at higher M_0 exciton edge in layer compound InSe. *Solid State Commun.* **28**, 439–443 (1978).
- Seabaugh, A. C. et al. In *Ultrafast Electronics and Optoelectronics* (eds J. Shah & U. Mishra) (OSA Proceedings Series, Optical Society of America, 1993).
- Capasso, F., Sen, S., Cho, A. Y. & Sivco, D. Resonant tunneling devices with multiple negative differential resistance and demonstration of three-state memory cell for multiple-valued memory applications. *IEEE Electron Device Lett.* **8**, 297–299 (1987).

29. Wei, S. J. & Lin, H. C. Multivalued SRAM CELL Using Resonant Tunneling Diodes. *IEEE J. Solid-State Circuits* **27**, 212–216 (1992).
30. Schmidt, P. et al. Nano-imaging of intersubband transitions in van der Waals quantum wells. *Nat. Nanotechnol.* **13**, 1035–1041 (2018).
31. Faist, J. et al. Quantum cascade laser. *Science* **264**, 553–556 (1994).

Acknowledgements

This work was supported by the Engineering and Physical Sciences Research Council [grant numbers EP/M012700/1 and EP/N033906/1]; the European Union's Horizon 2020 research and innovation programme Graphene Flagship Core 2 under grant agreement number 785219; the Defence Science and Technology Laboratory (Dstl); the University of Nottingham; The National Academy of Sciences of Ukraine; The Leverhulme Trust [RF-2017–224]; and The Royal Society [IE160395]. E.E.V. acknowledges the support from the Russian Science Foundation (17–12–01393). A.P. acknowledges the Chinese Academy of Sciences (CAS) for the Award of a “President's International Fellowship for Visiting Scientists”.

Author contributions

J.K. fabricated the devices; Z.R.K., E.E.V. and O.M. conducted the transport measurements; Z.R.K., J.K. and D.M. conducted the optical studies; J.K. conducted the AFM studies; Z.R.K. and Z.D.K. grew the bulk InSe crystals; Z.R.K., E.E.V., O.M., L.E., P.H.B. and A.P. analysed and interpreted the experimental data; M.T.G. developed a model to describe the transport properties of the devices. A.P. wrote the paper; all authors took part in the discussion and analysis of the data.

Competing interests

The authors declare no competing interests.

Additional information

Supplementary information is available for this paper at <https://doi.org/10.1038/s42005-020-0290-x>.

Correspondence and requests for materials should be addressed to A.P.

Reprints and permission information is available at <http://www.nature.com/reprints>

Publisher's note Springer Nature remains neutral with regard to jurisdictional claims in published maps and institutional affiliations.



Open Access This article is licensed under a Creative Commons Attribution 4.0 International License, which permits use, sharing, adaptation, distribution and reproduction in any medium or format, as long as you give appropriate credit to the original author(s) and the source, provide a link to the Creative Commons license, and indicate if changes were made. The images or other third party material in this article are included in the article's Creative Commons license, unless indicated otherwise in a credit line to the material. If material is not included in the article's Creative Commons license and your intended use is not permitted by statutory regulation or exceeds the permitted use, you will need to obtain permission directly from the copyright holder. To view a copy of this license, visit <http://creativecommons.org/licenses/by/4.0/>.

© The Author(s) 2020